PHYSICAL REVIEW B **107**, 155139 (2023)

Band structure of a nonparabolic two-dimensional electron gas system

Dawid Wutke,[1] Mariusz Garb,[1] Agnieszka Krawczyk,[1] Anna Mielczarek,[1] Natalia Olszowska,[2] Marcin Rosmus,[2]
and Jacek J. Kolodziej[1,2,*]

[1]*Faculty of Physics, Astronomy and Applied Computer Science, Jagiellonian University, Lojasiewicza 11, 30-348 Kraków, Poland*
[2]*National Synchrotron Radiation Centre SOLARIS, Jagiellonian University, Czerwone Maki 98, PL-30392 Kraków, Poland*

(Received 15 July 2022; revised 9 December 2022; accepted 11 April 2023; published 25 April 2023;
corrected 4 May 2023)

Using angle-resolved photoelectron spectroscopy (ARPES), we study the band structures of two-dimensional electron gases (2DEGs) formed at Te-doped surfaces of InAs(110), as a result of band bending. The selected surface system is very clean and stable; therefore, ARPES spectra may be registered in short times, with minimal adsorption of residual gases and no photon beam-induced damage. We record a set of data that allows for a detailed analysis of the 2DEG band shapes, their thermal dependencies, and for an assessment of the many-body interactions. We find the electron-phonon interaction extremally weak and the electron-electron interactions hidden in dominant electron-donor interactions. While 2DEG band shapes are observed to be variable in correlation with the 2DEG density, this is tracked down to the variability of the band-bending potential and nonparabolicity of the system, and not to the many-body interactions. Thus, many-body renormalization of the 2DEG bands is not required, and the bands are described well by using the one-electron theoretical frame.

DOI: 10.1103/PhysRevB.107.155139

I. INTRODUCTION

Two-dimensional electron gases (2DEGs) at III-V semiconductor interfaces are irreplaceable components of electronic technology today [1–6] and are also highly prospective for the realization of quantum information [7–17] and spintronic devices [18–20]. Furthermore, they are fascinating objects from the point of view of fundamental knowledge, hosting many interesting and often not well-recognized phenomena characteristic of electronic systems with reduced dimensions [21–26].

2DEG systems are formed with interfaces and surfaces confining electrons to a thin layer. In semiconductors, the confining action may also be realized with a single, electrically charged interface and surface (or a device gate) that is associated with the Thomas-Fermi screening and the band bending. Such "band-bending 2DEGs" are working in many devices [2,27,28]. Within our interest are the band-bending 2DEGs at surfaces since their band structures are exposed to be studied directly, with the use of angle-resolved photoelectron spectroscopy (ARPES).

One of the materials studied most frequently, in the context of surface 2DEGs, is InAs [29–35]. In this paper, we use ARPES to investigate 2DEGs formed at the Te-doped surface of InAs in great detail. We have selected these systems after extensive searches as being very robust and clean, providing reliable data, and also enabling 2DEG density control. Moreover, the systems may be regenerated many times, being thus suitable for complex experiments, such as temperature-dependent studies. An interesting circumstance is that, given the large InAs Bohr radius of ≈34 nm and the prevailing density found within 15 nm of the surface, the systems do not depart far from the ideal two-dimensionality.

II. EXPERIMENT

Experiments are carried out at the URANOS beamline at the National Synchrotron Radiation Centre SOLARIS in Krakow. The base pressure in the experimental system is 4×10^{-11} mbar. InAs(110) substrates are obtained by cleaving in UHV a degassed piece of a nominally undoped InAs (001) wafer, squeezed between two Mo sheets spot welded on a transferable sample plate. The wafer is n type, with a residual donor concentration of 3×10^{16} cm^{-3} (MTI supplier data). The samples are adsorbed with Te from a quartz-crystal microbalance-calibrated effusion cell and then annealed in steps to an increasingly higher temperature, for 30 min, starting from 500 K. The preparation process has been also tracked with the low-energy electron diffraction (LEED) and x-ray photoelectron spectroscopy (XPS) techniques.

The cleaved sample surface covered with a ~1 ML of Te shows off (1×1) LEED image with a substantial incoherent background. Upon annealing, the system undergoes complex transformations, which is seen, from the LEED perspective, in the following way (Fig. 1): $(1 \times 1) \xrightarrow{600\text{ K}} (3 \times 1) \xrightarrow{750\text{ K}} (n \times 1) \xrightarrow{775\text{ K}} (3 \times 1)' \xrightarrow{800\text{ K}} (1 \times 1)'$. With the help of XPS peak intensities and chemical shifts [Figs. 2(a)–2(c)], we can state that the initial Te (1×1) overlayer transforms sequentially into surface alloy phases: (3×1), $(n \times 1)$, $(3 \times 1)'$, having ~60% surface Te content, and then the Te is lost from the surface by thermal desorption. This last transition is seen as the gradual disappearance of fractional order LEED spots, meaning the decay of the $(3 \times 1)'$ alloy phase, in favor of the $(1 \times 1)'$ phase. The final $(1 \times 1)'$ phase shows Te content

---

[*] jj.kolodziej@uj.edu.pl

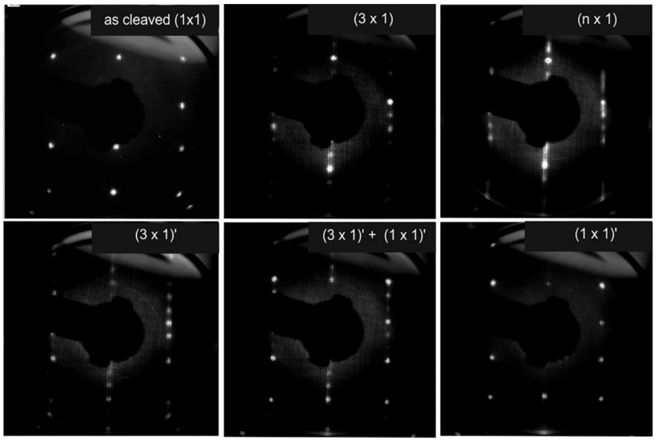

FIG. 1. LEED images for the as-cleaved surface and for the TE-dosed and annealed surface. Labels indicate the Wood's designations of the LEED patterns.

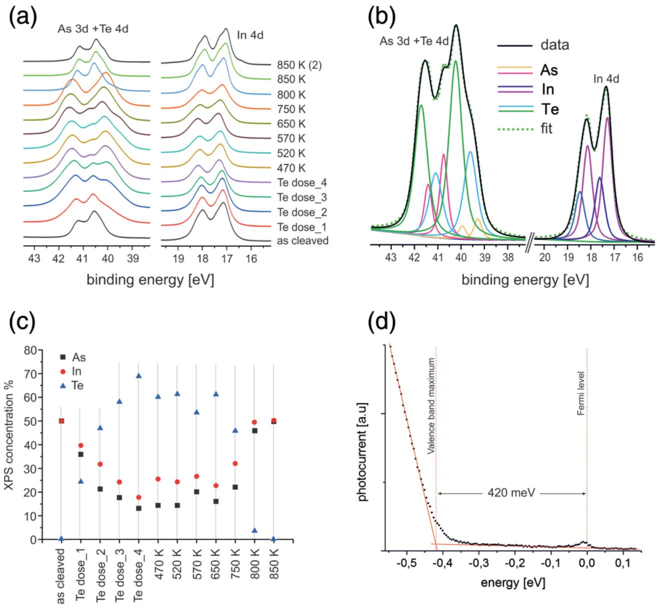

FIG. 2. (a) Sequence of XPS spectra showing the surface system evolution during Te deposition and annealing. (b) An example of the XPS spectrum decomposition for the chemical analysis of the surface. The spectra are decomposed using Voigt line shapes. Surface and bulk components have to be assumed for each element. The number of free parameters is reduced as far as possible, based on reference spectra for the as-cleaved InAs and the thick Te film. The following parameters are fixed (numbers given in order: for As; for Te; for In): relative sensitivity factor: 1.00; 1.80; 1.80, spin-orbit splitting: 0.67; 1.49; 0.85 (eV), spin-orbit split peaks area ratio: 1:60; 1.36; 130, FWHMs: 0.40; 0.77; 0.49 (eV). (c) Surface XPS elemental concentrations obtained by decomposition of the spectra in (a). (d) Photoelectron spectrum around the Fermi level for the as-cleaved sample at 80 K. The valence band maximum (VBM) position is obtained as an onset of valence photoelectron signal as shown. The VBM is seen 420 meV below the Fermi level. Given the fundamental gap of InAs at 80 K being 404 meV and the expected Fermi level 12 meV above the conduction band minimum (CBM), this result evidences the flat-band condition.

of the order of 1%. ARPES shows that the surface includes weak nondispersive bands (at −1 eV and at −1.5 eV, spectra not shown), nonexistent for the cleaved substrate, indicating a random distribution of the Te atoms. We conclude that the final $(1 \times 1)'$ phase is an ordered, unreconstructed surface of InAs(110) with a random Te donors substituting As within the top atomic layer.

The freshly cleaved InAs(110) surface shows the flat bands condition and does not contain 2DEG [see Fig. 2(d)], in agreement with previous studies [32,35,36]. The 2DEG is seen readily after Te deposition; however, the signals are weak, likely due to final-state scattering of photoelectrons on a not well-ordered surface. The (3×1) surface alloy phase is crystallographically ordered and produces a resonable 2DEG signal; but, on this surface photoelectrons get umklapp scattered in their final states and the photoelectron streams are divided into several replicated 2DEG bands. While not used for the main experiment, this surface was useful for precise calibration of the k scale for our experiments. For the core studies presented in this paper, we use the $(1 \times 1)'$ surface due to the superior 2DEG ARPES signals observed for this surface and because the 2DEG density, tied to the surface Te content, can be controlled on this surface in a wide range, by thermal annealing.

Since band bending of semiconductors is highly sensitive to adsorption of residual gases, to photon beam induced damage, and so on, care is taken to ensure that the sample surface state is unchanging during the experiments, both in short and long terms. The ARPES spectra are recorded on freshly prepared or refreshed samples. An acquisition time of a single ARPES 2DEG spectrum is reduced to 2 min, and typically five spectra in a row are taken for given experimental parameters. The measurement is accepted as valid only if the spectra do not differ. During the thermal study, before moving to the next temperature point, the surface was refreshed by thermal annealing to 723 K for 30 min. The study, which lasted around 2 days, contains two cycles over the measured temperature range and shows good repeatability (see also the Supplemental Material [37]).

ARPES spectra are recorded with the SCIENTA DA30-L photoelectron spectrometer, having a maximum angular resolution of 0.1°. The sample is held and oriented on a PREVAC five-axis cryogenic manipulator. The temperature obtainable on a copper sample holder block with LHe cooling is 6 K.

The Fermi level is determined with a Gaussian-Fermi convolution fit to the experimental Fermi steps. With smooth data acquired at cryogenic temperatures, the accuracy of such a procedure is better than 1 meV. Furthermore, the thermal sequences are measured with a monochromator staying in a constant position, also providing long-term photon energy stability ∼1 meV. Thus, the precise Fermi energy, found for cryogenic temperatures, is valid also for higher-temperature spectra. This, however, requires an additional justification: On semiconductors under photon beams, most often at cryogenic temperatures, photovoltage effects are observed, causing the appearance of temperature-dependent quasi-Fermi levels [38–40]. In order to avoid errors related to such effects we have investigated the external Fermi level on a polycrystalline gold reference sample. At 7 K we have observed a minute Fermi step shift (2.5 meV to lower energies) relative to the external Fermi level. Photovoltage effects decrease with increasing temperature [41]. At 80 K no measurable photovoltage effect has been seen, so we conclude that the Fermi level measured at 80 K and above is unaffected. Also, at 7 K, a minute decrease in the 2DEG density (by 15%), due to carrier freeze-out on surface donors, is observed (see also Sec. IV C). Therefore, the temperature-dependent results are interpreted only within the limited temperature range 80–470 K.

Due to radiation and thermal resistances, the sample surface temperature differs from that measured on the copper sample holder block. From a detailed Fermi step fit at the minimal obtainable temperature, we have found both the true sample surface temperature (10–11 K) and the spectral resolution (8 meV). Having this, we can also estimate the temperature errors for other temperatures, by scaling thermal radiation fluxes. Up to room temperature, the error decreases from 4–5 K to zero, and then it is reversed. At a maximum measured temperature of 470 K, the true temperature is, in this way, estimated to be 445 K. As seen, the relative temperature errors are not large and, if not indicated otherwise, in our discussion, we use uncorrected temperatures.

III. THEORETICAL CONSIDERATIONS

The band-bending 2DEG problem is modeled with a set of coupled Poisson and Schrödinger (SP) equations, set in planar geometry. To solve the problem, the effective mass approximation and the Thomas-Fermi (TF) method are applied [42–45].

For ease of calculation, we use an approximate, analytic form of the Kane **kp** dispersion relation [45,46]

$$E_{\mathrm{cb}}(k^2) = \frac{\hbar^2}{2m_0}k^2 + \frac{E_g}{2}(\sqrt{1+4P^2k^2}-1),$$
$$P^2 = \frac{3\hbar^2}{2m_0}\left(\frac{m_0}{m_{\mathrm{cb}}}-1\right)\frac{E_g+\Delta}{(3Eg+2\Delta)E_g}, \tag{1}$$

where E_g is the band gap parametrized with the Varshni formula [47], the zero energy is set at the band minimum, m_0 is the free-electron mass, Δ stands for the spin-orbit coupling ($\Delta = 0.381$ eV in InAs), and m_{cb} is the band-edge effective mass of electrons, hereafter referred to as the conduction band mass (or simply the band mass). For m_{cb}, we should use the estimate of InAs empty band effective mass, that is, $0.023m_0$ [48]. However, while the approximated bands described by Eq. (1) have been used by different authors (and also in our earlier work) for the InAs crystal [22,45,49], we have noticed now that their parabolic characteristics around minimum are not consistent with the m_{cb} (the Kane band, near minimum follows: $\hbar^2k^2/2m_{\mathrm{cb}}$). This (minor) problem is easily fixable. Within the region of our interest we have compared Eq. (1) with the genuine Kane **kp** InAs conduction band [50]. They converge almost exactly (to within 0.5 meV) if the mass $m_{\mathrm{cb}}^{\mathrm{corr}} = 0.02685m_0$ is used in (1), instead of the standard $m_{\mathrm{cb}} = 0.023m_0$. In further analysis, we apply the corrected mass whenever Eq. (1) is involved, that is, effectively we use the proper InAs Kane bands.

The local electron density, in the TF approximation, is

$$n_{\mathrm{cb}} = \frac{1}{\pi^2}\int_0^\infty \frac{k^2\,dk}{1+\exp\{\beta[E_{\mathrm{cb}}(k)-E_F+V(z)]\}}, \tag{2}$$

where k_B and E_F have their conventional meaning, $\beta = 1/k_BT$, $V(z)$ is the electron potential energy. Holes are of minor meaning here, and their local density is calculated using approximate parabolic dispersion relations, sufficient close to Γ:

$$p_i = \frac{1}{\pi^2}\int_0^\infty \frac{k^2\,dk}{1+\exp\left[\beta\left(E_g+\frac{\hbar^2}{2m_i}k^2+E_F-V(z)\right)\right]}, \tag{3}$$

where $i \in \{lh, hh\}$ concern light and heavy holes of masses $0.021m_e$ and $0.41m_e$, respectively.

The electron neutrality condition in a deep bulk [where $V(z) = 0$] is

$$p_{lh} + p_{hh} + p_d - n_{\mathrm{cb}} = 0, \tag{4}$$

where p_d is the spatial density of the ionized donors.

Then the Poisson equation is formulated

$$\frac{d^2}{dz^2}V(z) = \frac{e^2}{\varepsilon_0\varepsilon_b}[p_{hh}(z)+p_{lh}(z)+p_d(z)-n_{\mathrm{cb}}(z)], \tag{5}$$

where ε_0 and ε_b are the vacuum dielectric constant and InAs static dielectric constant, and e is the elementary charge. We require that $V(0)$ is equal to the total band bending (BB) and that $V(z)$ vanish deep in the bulk $p_d(z)$. The set of equations (1)– (5) is solved to find $V(z)$.

To find 2DEG wave functions and energies, the Schrödinger equation is written

$$[E_{\mathrm{cb}}(\nabla^2) + V(z)]\psi = E\psi, \tag{6}$$

where ψ are wave functions of 2DEG: $\psi = \psi(x, y, z, k_x, k_y) =: \psi(\mathbf{r}_\parallel, z, \mathbf{K}_\parallel)$. Counterintuitively, while the k_z quantum number is nonexistent, the complete separation of the problem into in-plane and out-of-plane parts is impossible (at least within the used description scheme) because of the nonparabolic kinetic energy operator. By the complete separation, we understand the situation where the in-plane and out-of-plane parts involve only in-plane and out-of-plane variables, respectively.

Therefore, it is written

$$\psi = \psi(\mathbf{r}_\parallel, z, \mathbf{K}_\parallel) = \psi_\parallel(\mathbf{r}_\parallel, \mathbf{K}_\parallel)\psi_\perp(z, \mathbf{K}_\parallel), \tag{7}$$

meaning that while the separation of space variables is still possible, it has to be done for each $\mathbf{K}_\parallel$ individually.

The following general boundary condition is set at the origin [51]:

$$\frac{d}{dz}\psi_\perp(0, \mathbf{K}_\parallel) = \lambda\psi_\perp(0, \mathbf{K}_\parallel), \tag{8}$$

and the λ is assumed to be not dependent on $\mathbf{K}_\parallel$. The λ accounts for the physical properties of the surface and is found at the end, by fitting the solution to the experimental data [22].

The following basis set is used:

$$\cos[kz + \phi(k)], \tag{9}$$

where the phase ϕ is dependent on k,

$$\phi(k) = \arccos\left[-\mathrm{sgn}(\lambda)\frac{k}{\sqrt{k^2+\lambda^2}}\right].$$

A dense grid of k values is set: $k_n = \frac{n\pi}{L}, L = 20\,000$, and the scalar product for the two "k_m" and "k_n" indexed vectors is defined as $\int_0^{2L}\cos[k_m+\phi(k_m)]\cos[k_n+\phi(k_n)]dz$. This constitutes an orthogonal basis set. Out-of-plane 2DEG wave functions (eigenfunctions) are represented as

$$\psi_\perp^i(z,\mathbf{K}_\parallel) = \sqrt{\frac{2}{L}}\sum_{n=1}^{\infty}a_{n,i}(\mathbf{K}_\parallel)\cos[k_n z+\phi(k_n)], \tag{10}$$

where the index "i" enumerates the 2DEG subbands. In the practical calculation, the sum is approximated with its first $n_{\max}$ elements (with the resulting $k_{n_{\max}}$ adequate to account for the spatial frequencies expected in the 2DEG envelope wave functions). In the present calculation, $n_{\max} = 2048$ has been found sufficient with a safe margin. Thus, the problem becomes reduced to the following matrix-eigenvalue equation [45,52]:

$$\sum_{n=1}^{n_{\max}} M_{m,n}(\mathbf{K}_\parallel)a_{n,i}(\mathbf{K}_\parallel) = E_i(\mathbf{K}_\parallel)a_{m,i}(\mathbf{K}_\parallel), \tag{11}$$

where the matrix elements are

$$M_{m,n}(\mathbf{K}_\parallel) = E_{\mathrm{cb}}\big(\mathbf{K}_\parallel{}^2 + k_n^2\big)\delta_{m,n} + \frac{2}{L}\int_0^\infty V(z)\cos[k_m + \phi(k_m)]\cos[k_n+\phi(k_n)]dz. \tag{12}$$

The "∞" integral limit is here an approximation for simplifying of the calculations. The scalar product for harmonic basis functions and the functions themselves are defined on a finite space, deep enough to have $V \approx 0$, at the right end. Formally, the integration should be done on the same space. Within our script, $V(z)$ is replaced with the precisely fitted linear combination of exponential functions, and so the integrals become analytical expressions. With L set to 20 000 the error due to replacing the $2L$ integral limit with ∞ is nonexistent.

The solution of the above matrix-eigenvalue problem yields the subband energies $E_i(\mathbf{K}_\parallel)$ and allows one to construct the wave functions $\psi_\perp^i(z,\mathbf{K}_\parallel)$, according to Eq. (10). The $\mathbf{K}_\parallel$ is treated, within this context, as a constant parameter. In order to find the 2DEG dispersion relations $E_i(\mathbf{K}_\parallel)$ the calculation is repeated for a grid of different $\mathbf{K}_\parallel$ parameters, covering the required range. Our experimental geometry warrants that $k_\mathrm{y} = 0$. Thus, the theoretical dispersion relations to be compared with experimental data are obtained by feeding the above equations with the $\mathbf{K}_\parallel{}^2 = k_\mathrm{x}{}^2$.

In the case of InAs 2DEG, the TF approximate solutions are very close to genuinely self-consistent solutions (cf. Refs: [45,52]). For more details regarding the SP calculations, see Ref. [22].

The above is the one-electron description of the 2DEG. It may be expanded to account for the many-body effects on the grounds of the quasiparticle theory. In this aspect, one may consider the complex self-energy $\Sigma = \Sigma_R + i\Sigma_I$.

ARPES measures the spectral function $A(\boldsymbol{k},\omega)$ which depends on the many-body self-energy components $\Sigma_{R,I}$:

$$A(\boldsymbol{k},\omega) \propto \frac{\Sigma_I(\boldsymbol{k},\omega)}{[\hbar\omega - \epsilon(\boldsymbol{k}) - \Sigma_R(\boldsymbol{k},\omega)]^2 + [\Sigma_I(\boldsymbol{k},\omega)^2]}. \tag{13}$$

$\epsilon(\boldsymbol{k})$ is here the one-electron band. The centroids of the experimental bands correspond to $\epsilon(\boldsymbol{k}) + \Sigma_R(\boldsymbol{k},\omega)$. The measured Lorentzian widths half-width at half-maximum (HWHM) of the bands are related to Σ_I. For a 2D system, the situation is particularly simple since the observed Σ_I directly reflects the scattering of the photohole state [53].

In the case of separable interactions, the $\Sigma_{R,I}$ may be represented as sums of partial self-energies: $\Sigma_{R,I}^{e\text{-}ph}$, $\Sigma_{R,I}^{e\text{-}e}$, and $\Sigma_{R,I}^{e\text{-}d}$, related to electron-electron (e-e), electron-phonon (e-ph), and electron dopant (e-d) interactions. In a further discussion, to interpret our experimental data, we will rely on the known properties of many-body interactions, that is, that e-ph interactions are decisive in the context of thermal dependence of Σ_I, and that the e-e and e-d interactions depend on the donor concentration [54]. Since the e-e and e-d interactions lead to similar experimental effects [55], we will also seek the support of the available theoretical papers to estimate the share of these interactions.

IV. RESULTS AND DISCUSSION

A. Survey studies and valence bands

In Fig. 3(a) we plot several survey spectra for the InAs(110):Te $(1\times1)'$ surface, acquired using different photon energies in the range 20–30 eV. k_x is a wave vector along KΓK path, which is also parallel to $(\bar{1}10)$ crystallographic direction [cf. Fig. 3(b)]. The 2DEG bands are seen just below the Fermi level, being the most intense for photon energies 24–26 eV. Below a −0.7-eV energy, the valence band states are found.

To conduct our experiments, we choose, based on the 2DEG signal intensity, the photon energy of 25 eV. This results in a very short photoelectron mean-free path (MFP) within the studied sample (~1 nm) and also in the extreme surface sensitivity of ARPES. Due to this and also to valence electron localization (on closed orbitals), the valence band signals come from the top 2–3 atomic layers. On the other hand, a short photoelectron state lifetime results in energy uncertainty, and somewhat complicated interpretation of ARPES results in the case of three-dimensional (3D) bands (e.g., valence bands). We explain this aspect in Fig. 4.

The valence bands of InAs, along the high-symmetry KΓK direction, may be obtained from the experimental data, with high precision. This is because the symmetries of the InAs lattice warrant that the KΓK is an extremal energy path, corresponding to a ridge or valley in the dispersion relation landscape. As shown in Fig. 4(b), with the proper choice of the photon energy, dispersion along such extremal path is reflected on ARPES spectrum as a sharp edge, limiting certain broad features. The geometry of our experiment [Fig. 3(b)] is chosen to exploit this scheme: the photon energy is scanned over a wide range [see Fig. 3(b) showing the essential part of the studied range]. With the photon energies 24–26 eV, the valence band features appear to be hardly changing, and their upper limits become sharp. This evidences that the "$\Delta k_\mathrm{x}\Delta k_z$"

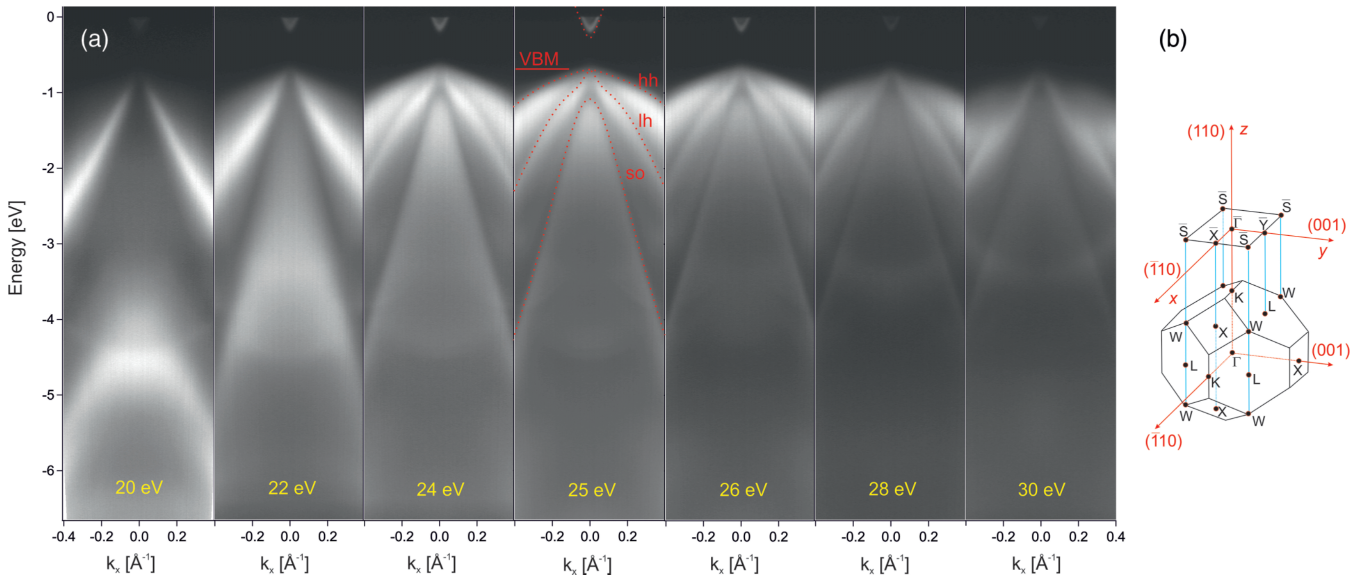

FIG. 3. (a) ARPES spectra for the Te-doped InAs(110) surface, acquired using several different photon energies (indicated at the bottom of each spectrum). k_x is a wave vector along $\bar{\Gamma}\,\bar{X}$ and also along ΓK [or ($\bar{1}$10) direction in real space]. Note that this direction and the direction normal to the surface (z) are crystallographically equivalent. Dotted red lines overlayed on the 25-eV spectrum denote calculated bulk InAs bands taken from Ref. [56]. (b) Bulk and (110) surface Brillouin zones for the InAs (zinc-blende) lattice with indicated symmetry points, main crystallographic directions, and the experimental xyz frame.

subspace, shifting along the k_z axis with changing photon energy, includes some extremal path. To verify that we are probing the desired KΓK path, we compare our spectra with the state-of-the-art calculations of InAs bands along KΓK path from Ref. [56]; see the lines overlayed on the 25-eV spectrum in Fig. 3. These bands fit closely to the upper edges of the observed spectral features, as expected. Advantageously, the obtained experimental band (the edge) is insensitive to k_z broadening and to moderate sample misalignments.

B. High-resolution 2DEG spectra

A representative 2DEG ARPES data set is presented in Fig. 5. The characteristic quantum-well band structure is

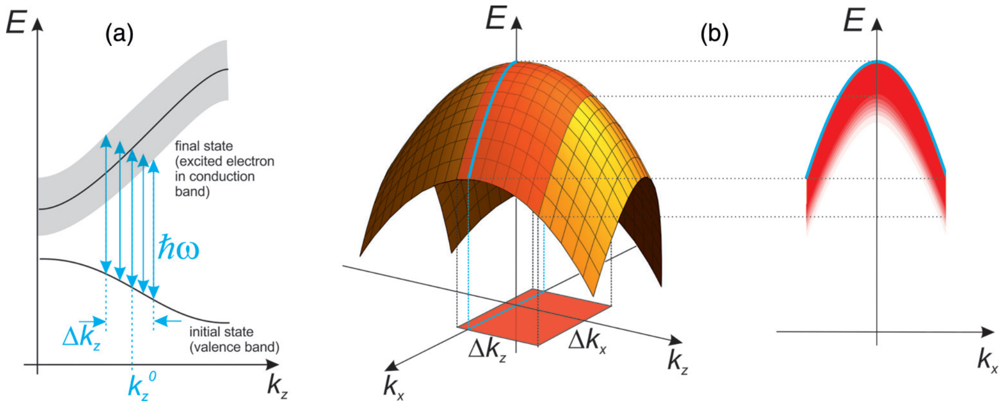

FIG. 4. (a) 3D electronic band in view of the three-step photoemission model (in the context of the "k_z-broadened" ARPES spectra). The initial state is assumed to be weakly broadened. The final state is strongly broadened as a result of short electron MFP; its uncertainty is denoted by a wide gray stripe. The photoelectron transition is vertical and connects the initial state with some final state, higher in energy by $\hbar\omega$ (the photon energy). This is possible in a certain range Δk_z, as indicated. The final state (which is actually an intermediate one when considering the complete photoelectric transition to the vacuum state) is not observed in ARPES; however, the relaxation of k_z constraints, caused by its uncertainty, does; it is Δk_z that determines the range of states observed with ARPES simultaneously, around a certain k_z^0 defined formally by the choice of the photon energy. (b) The "k_z projection" to obtain the ARPES spectrum of a 3D band. The experimental geometry warrants $k_y = 0$. The Δk_x range is determined by the angular acceptance of the electron spectrometer, specifically by its slit length, lens voltages, etc. The rectangular red field denotes the part of (k_x, k_z) space that contributes to the spectrum (in reality, it is not exactly rectangular; it has been drawn like that for simplicity). The ARPES spectrum is obtained by projecting the relevant part of the dispersion relation $E(k_x, k_z)$ onto the plane (E, k_x) as schematically indicated. The blue line is drawn along the extremal energy path ($k_z = 0$), which corresponds to a ridge in the dispersion relation landscape.

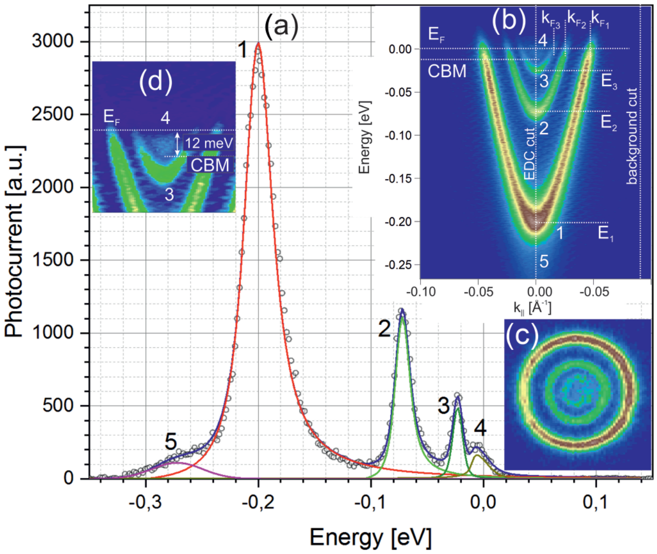

FIG. 5. High-resolution ARPES data for 2DEG at the InAs(110):Te surface, at $T = 80$ K. (a) Energy distribution curve (EDC) of photoelectrons emitted normal to the surface. The fitted model and its elemental constituents are shown using lines of different colors. (b) ARPES image of bands with marked relevant energy levels, Fermi wave vectors, cuts, etc. (c) Fermi surface. (d) Enlarged and optimally contrasted detail that exposes the bulk conduction band feature. The position of the bulk conduction band minimum (CBM) is shown, calculated based on the residual doping level of the wafer.

observed. Far from their minima, the 2DEG bands appear as almost straight lines, resembling the Kane **kp** bands [50] observed for bulk conduction bands of narrow-gap III-V semiconductors.

The Fermi surfaces [Fig. 5(c)] are circularly symmetric, so the 2DEG sheet density can be obtained with the Luttinger area rule, as $n_{\mathbf{2D}} = \sum_i k_{F_i}^2/(2\pi)$, where $k_{F\,i}$ are Fermi wave vectors measured for the 2DEG bands [see Fig. 5(b)]. Since we use the lightly doped (nominally undoped) InAs substrate and the untreated surface displays the flat bands, 2DEG electrons come predominantly from the surface Te donors introduced during the surface preparation. Therefore, the sheet 2DEG electron density and the surface donor concentration have to be approximately equal in our systems.

The energy distribution curve (EDC) of photoelectrons emitted along the normal to the surface is shown in Fig. 5(a). Peaks 1, 2, and 3 correspond to the minima of the 2DEG bands. The vague feature 4 may reflect the higher 2DEG subbands or the bulk conduction band. Shoulder 5 is a shake-off plasmon feature that has been observed before [57,58]. Analogous satellites at peaks 2 and 3, with their intensities proportional to the parent peak area, are lost in the data noise. We do not discuss these secondary features further. The position of the conduction band minimum (CBM) is marked 12 meV below the Fermi level, determined with Eq. (4) under the assumption of full donor ionization. The 2DEG peaks have a dominant Lorentzian character (i.e., wide bases), indicating that lifetime effects mostly determine their shapes. Due to the $k_\|$ experimental uncertainty, some moderate asymmetries are seen in the shapes of 2DEG peaks. With a trial-and-error procedure, we have developed line shapes based on Voigt functions that ensure the reliable fitting of our 2DEG peaks (cf. the Supplemental Material for a description of the line shapes [37]). The background is subtracted from the experimental data prior to the fitting. The Gaussian FWHMs of all Voigt peaks are fixed on the experimental energy resolution (8 meV). The model spectrum is constructed by adding all components together and multiplying the sum with the Fermi distribution [cf. Fig. 5(a)]. After the fits converge, the energies of the band minima, Lorentzian widths, etc., are read from among the fit parameters.

C. Temperature dependencies in the 2DEG spectra

The ARPES spectra of 2DEG at the Te:InAs(110) $(1\times1)'$ surface measured at a few different temperatures are shown in Fig. 6. No measurable thermal dependencies are found in the band shapes. In the temperature range 80–463 K, a small monotonous increase of 2DEG band energies is observed (in the Fermi level frame). Upon temperature rise, the degenerate semiconductor becomes nondegenerate somewhere between 80 and 180 K. This is typical (textbook) behavior of the n-type InAs semiconductor.

A separate case is the “7-K” spectrum. The 7-K 2DEG bands are shifted up as compared to the “81-K bands.” This is an indication of carriers freeze-out on surface donors. The magnitude of the effect is estimated by comparing the 2DEG Luttinger area for 7 and 81 K, leading to the result that only 15% of the carriers are frozen out upon cooling down the surface to ≈10 K. Since the freeze-out is a thermally (de)activated process, for much higher temperatures (within the range 80–470 K) the freeze-out effects can be safely neglected.

D. Electron-phonon interactions

When the temperature changes, the dominant variation of Σ_I is due to its $\Sigma_I^{e\text{-}ph}$ component. The electron-accoustic-phonon interaction (e-ph) is quantified with the coupling constant $\lambda_{e\text{-}ph}$. This constant may be evaluated based on the thermal dependence of the electronic-band energy width. We have studied the band 2, for which the width changes are the most clearly seen, at its minimum, where the $dE/dk_\| = 0$ and so the k uncertainty is not involved. At the band minimum the possible complications caused by spin splitting [59] are absent as well. The result is shown in Fig. 7.

According to the Debye model, above the temperature $\Theta_D/3$ [60] (Θ_D is the Debye temperature), the ARPES bandwidth (in energy) should increase approximately linearly with temperature, with the slope matching the $2\pi k_B\lambda_{e\text{-}ph}$ [61]. The InAs Θ_D is ≈280 K so the line fit (see Fig. 7) is justified within the whole measured range 80–470 K. With the fit we find $\lambda_{e\text{-}ph}$=0.034(2) (this result is corrected for the estimated temperature error). Now, the band renormalization component $\Sigma_R^{e\text{-}ph}$ may be estimated, again with the help of the Debye model. According to the model the $\Sigma_R^{e\text{-}ph}$ increases approximately linearly from zero at the Fermi level, reaches some maximal value limited by $\lambda_{e\text{-}ph}k_B\Theta_D$, at the energy $-k_B\Theta_D$, and quickly drops to zero for lower energies [62,63]. We obtain the $\Sigma_R^{e\text{-}ph}$ limit as 0.9 meV so it is evi-

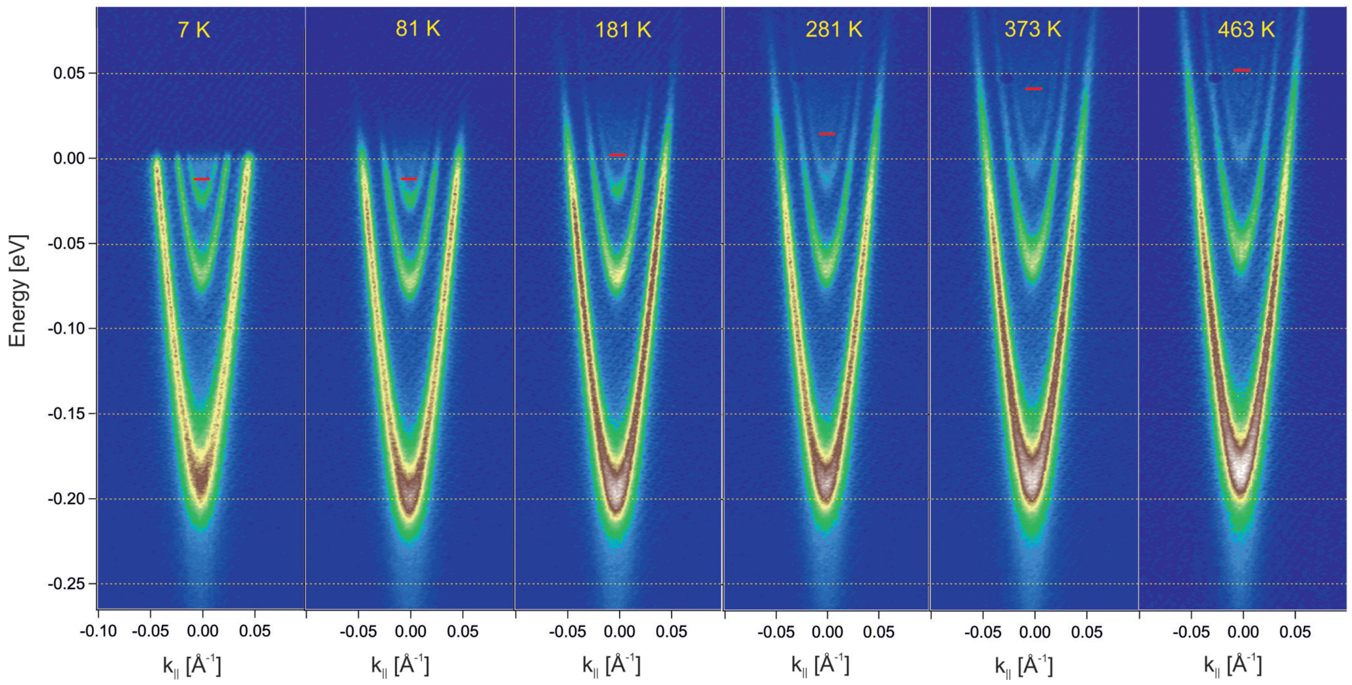

FIG. 6. ARPES spectra of 2DEG at the Te:InAs(110) $(1\times1)'$ surface illustrating the thermal dependence of the 2DEG electronic structure. The spectra are labeled with temperatures measured on the sample holder. True surface temperatures may differ insignificantly as compared to these measured temperatures. Red marks indicate the position of the bulk conduction band minimum calculated using Eq. (4) in Sec. III, under the assumption of full donor ionization.

dent that the electron-phonon-related band renormalizations (expected around the Fermi level) are unnoticeable within our ARPES data. No signatures [64] of electron-longitudinal-optical-phonon (Fröhlich) interactions have been seen either.

E. Electron-electron and electron-donor interactions

To study many-body interactions beyond the electron-phonon interactions, we have prepared a set of samples with 2DEG sheet densities in a broad range. The ARPES data for the set are shown in Fig. 8. With these spectra, we have measured or evaluated several parameters of the 2DEGs; we list them in Table I. The *e-e* interactions are characteristically reflected in the dependence of the width of the electronic bands on energy. The width is described with the following formula: $\Gamma_{e\text{-}e}(=2\Sigma_I^{e\text{-}e}) = 2\beta[(\pi k_B T)^2 + E^2]$, where β is a constant. The formula is given for 3D systems; however, it can also be used to estimate the order of magnitude of the interaction in 2D [65]. We also use an approximate rule for calculating β, given in the work of Quinn and Ferell [66]: $\beta_{\text{QF}} = r_s^{5/2}/263$ (eV^{-1}). The expected magnitudes of the $\Gamma_{e\text{-}e}$ using the r_s values given in Table I are below 10^{-5} eV.

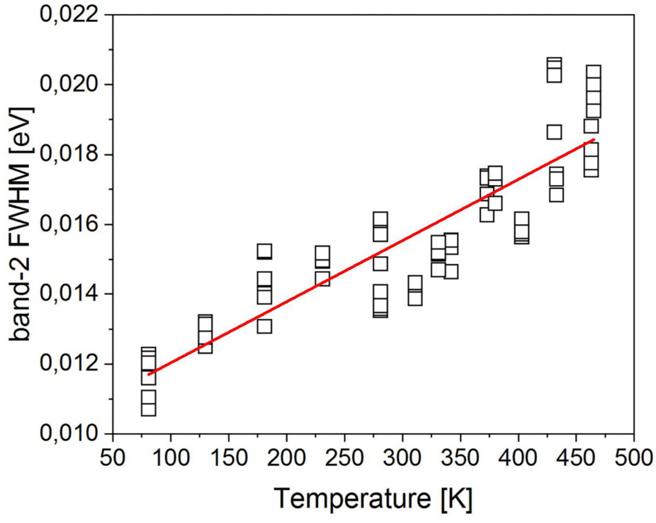

FIG. 7. EDC Lorentzian width of band 2 at minimum vs temperature with fitted linear trend, denoted by the solid red line.

e-e interactions may be somewhat increased in 2D systems compared to 3D systems [21,67], but experimentally observed Lorentzian widths of the 2DEG bands (Table I) are still 2–3 orders of magnitude too large to be explained with these interactions. The widths cannot be explained with the

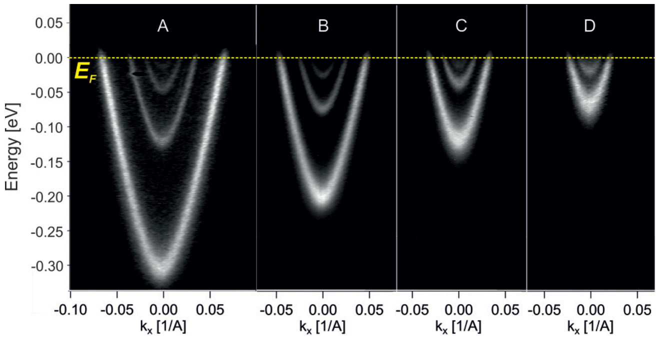

FIG. 8. ARPES spectra of 2DEG at the InAs(110):Te surface, for several different densities (or Te surface content) at $T = 80$ K.

TABLE I. Measured and evaluated 2DEG properties for a few samples with different 2DEG densities. E_i are the band minima energies in the Fermi level frame. Γ_i are Lorentzian energy widths (FWHM) at the 2DEG band minima. k_{Fi} are Fermi wave vectors; see Fig. 5. The sheet electron density n_{2D} is obtained as the Luttinger area. The Wigner-Seitz r_s density parameter is evaluated on the basis of n_{2D}. The VBM is obtained as an onset of the valence band signal in angle-integrated ARPES spectra. BB is the total band bending obtained with the formula: BB $= -$VBM $-$ CBM $- E_g$). The uncertainties are ±2 meV and ±25 meV for the energies E_i and VBM/BB, respectively.

Sample	A	B	C	D
E_1 (meV)	-308	-202	-121	-74
E_2 (meV)	-121	-73	-38	-25
E_3 (meV)	-46	-24	-12	
E_4 (meV)	-11		–	
Γ_1 (meV)	30	28	33	32
Γ_2 (meV)	12	12	13	13
Γ_3 (meV)	7	6		
$k_{\mathrm{F_1}}$ (Å^{-1})	0.066	0.046	0.032	0.021
$k_{\mathrm{F_2}}$ (Å^{-1})	0.035	0.025	0.017	0.011
$k_{\mathrm{F_3}}$ (Å^{-1})	0.029	0.013	0.008	
$k_{\mathrm{F_4}}$ (Å^{-1})	0.008			
VBM (meV)	-910	-755	-625	-540
BB (meV)	495	340	210	125
n_{2D} (10^{12}/cm^2)	9.6	4.7	2.1	0.9
2D r_s	0.11	0.15	0.23	0.35

e-ph interactions either since the widths are observed to be variable, while the $\Sigma_I^{e\text{-}ph}$ is constant below the energy $-k_B\Theta_D$, i.e., below −24 meV, in the case of InAs. Thus, we are left with the *e-d* interactions as the only possible explanation of the bandwidths. Looking through the widths for all samples, we immediately see that they depend mainly on the band number. This is consistent with the dominant contribution of *e-d* interactions; the sequence of potential screening [cf. Fig. 9(c)] causes the photoholes residing in the higher subband to be less probable to scatter on potential variations induced by the ionized donors residing in the top atomic layer, as compared to the photoholes of the lower subband. This result (i.e., dominant interactions of the *e-d* type) is actually not very surprising, given the abundant evidence, obtained by measuring extremally high carrier mobilities (implying weak scattering) in III-V-based 2D systems [27,68–71]. The mobilities are limited only by the presence and proximity of dopants and impurities, which also indicates that the dominant interactions in these systems are of *e-d* type.

To further analyze the interactions, we present Fig. 9(a). The figure shows digitized centerlines of electronic bands observed for samples of different 2DEG densities, together with a few model lines, which we discuss below. The shapes of the 2DEG bands change with the 2DEG sheet density. They appear to be Kane type, so we have fitted the lowest bands with the Kane shapes, keeping the bulk values of E_g and Δ, just to parametrize the band lines. Surprisingly, by allowing only free m_{cb}, almost perfectly accurate fits are obtained: they are shown in Fig. 9 with solid black lines. The fitted masses are shown in Table II. The same masses are obtained with fitting parabolas close to band minima, so we will use the term "band mass" for these parameters. The data show an increase in band mass, with reference to the standard InAs

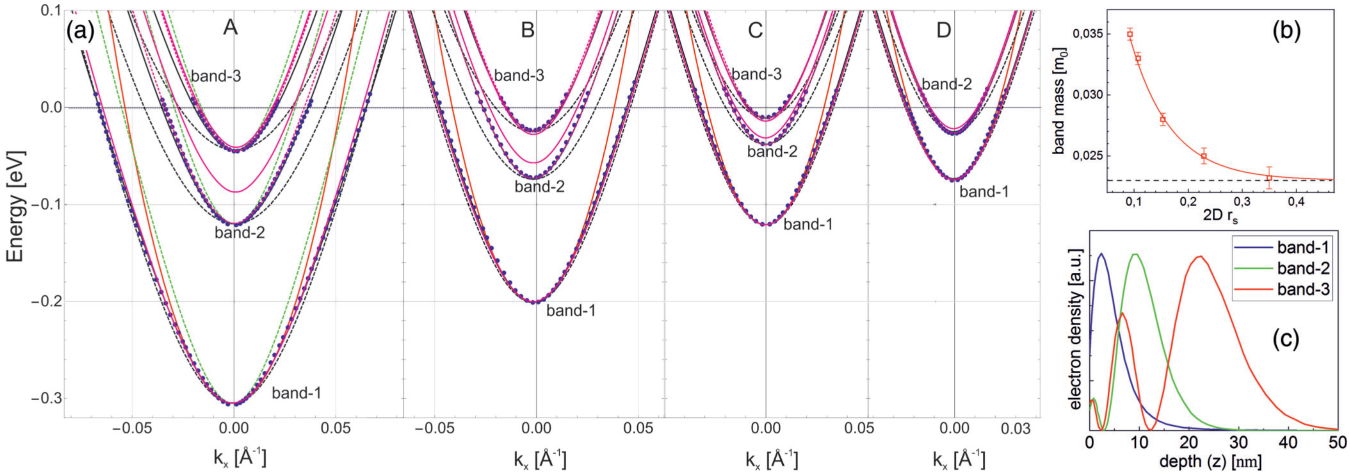

FIG. 9. (a) Centerlines of 2DEG bands for several differently doped InAs(011):Te surfaces: points. The data marker size corresponds to the experimental uncertainty. Solid black lines are Kane bands fitted to the experimental band 1's, and the red lines are parabolas fitted around the band minima. The solid black lines at bands 2 and 3 are obtained by vertical translations of the band-1 lines. The green dashed lines on the A panel show the Kane band shapes, corresponding to a 3D InAs conduction band, and also being very close to the band shapes of sample D. The black dashed lines show the Kawasaki *et al.* model bands. Solid magenta lines show the SP/TF (Schrödinger-Poisson/Thomas-Fermi) bands found as the solutions to Eq. (11) (Sec. III). Dashed magenta lines show SP bands 1 and 2 shifted closer to the experimental bands to better visualize their convergence in shape. The SP/TF band 1's are forced to fit to the experimental band minimum by choosing the boundary parameter λ. The λ equal to 0.048 has been found in this way, common for all samples. Note that the magenta lines, added as the top figure layer, often coincide with the solid black lines and cover them. (b) Dependence of the Kane band mass vs the two-dimensional Wigner-Seitz r_s parameter, well described with the shown exponential decay line, asymptotically corresponding to the mass $0.023m_0$. (c) Probability distributions for 2DEG states (at $\mathbf{K}_\parallel = 0$) calculated within the SP/TF scheme, concerning sample A, normalized to their maxima.

TABLE II. Fitted Kane **kp** band masses. The uncertainties are ± 0.0005.

Sample	A	B	C	D
kp (Kane) mass (m_0 unit)	0.033	0.028	0.025	0.023

band mass, reaching 43% for the most dense 2DEG studied. When represented as a function of the Wigner-Seitz 2D r_s parameter, the mass shows a monotonic decrease, approaching the asymptotic value [72] of $0.023m_0$ for $r_s > 0.4$ [see Fig. 9(b)]. This is equal to the standard band mass of InAs. The asymptotic band mass is correlated with the vanishing 2DEG density, i.e., with vanishing many-body interactions, but also with vanishing significance of nonparabolicity of the bands; thus, both many-body interactions and nonparabolicity may, in principle, be the cause of the observed mass variation. The band shapes do not depend on the band number (to the experimental accuracy), so all subbands, for a given sample, are fitted well with the single band shape (see Fig. 9).

At first let us discuss the predictions, which specifically relate to changes in band mass, resulting from the *e-e* interactions. On the basis of our earlier estimations concerning the $\Sigma_I^{e\text{-}e}$ we expect them being not very significant. The relevant theoretical predictions may be also read in Ref. [73], where the enhancement of the effective mass in 2D electron liquid is given, based on a few different models. For the relevant range of r_s, a decreasing effective mass (at the Fermi level) is found with increasing r_s, but the total change is less than $0.0005\ m_0$. Studying the quasiparticle self-energy vs k curves characters, provided in Ref. [73] one finds that the effect around $k = 0$, i.e., on the band mass must be less than that. Thus, our observations cannot be explained with *e-e* interactions (and in fact, the predicted interactions are far too weak to cause any effect on the $\Sigma_R^{e\text{-}e}$, observable with our technique).

Concerning *e-d* interactions, the standard assumption is that they lead only to rigid shifts of electronic bands [74,75], so that no band mass renormalization is expected. On the other hand, there exists an experimental report on the band-edge mass increase (by 14%) on a heavily doped (up to $8 \times 10^{18}/\mathrm{cm}^3$) GaAs [76]. Also, in a recent theoretical paper [77], with the help of *ab initio* calculations of the *e-d* interactions in Si, it has been concluded that, contrary to conventional wisdom, carrier scattering may depend strongly both on the type of defect and the carrier energy, which could lead to the renormalization of the band mass. While we cannot exclude such effects completely for our 2DEG system, we will show below that they are not the leading-order ones.

F. One-electron effects on 2DEG band shapes

Beyond the many-body interactions, other mechanisms are possible to explain variation in band shapes in the 2DEG systems. One is based on the observation that the electron wave function spills out beyond the confining barriers, and thus the electron acquires, to some extent, properties characteristic of the outer medium. A simple rule to estimate the mass in such circumstances, based on a probability distribution between the quantum well and the outer medium, is given in Ref. [78] by Schildermans *et al.* Using this rule, and taking the InAs(110) work function of 4.9 eV [79], we determine the exponential decay length of the electron wave function in vacuum, and then, with the solution shown in Fig. 9(c), assuming the smooth wave function, we evaluate the expected mass enhancements for sample A (for which the effect would be the most pronounced). The enhancements are $\leqslant 0.002$, $\leqslant 0.0003$, and $\leqslant 0.0002$ (in m_0 units) for bands 1, 2, and 3, respectively. Thus, we see that the "spillout" could contribute marginally to the observed mass of band 1 only (see also the Supplemental Material for more discussion on this topic [37]).

Another mechanism has been proposed for the variable masses observed for nonparabolic electron subbands of ultrathin $\mathrm{IrO_2}$ films by Kawasaki *et al.* [24]. They stated that for 2D "*i*" metallic band, one may associate formally a constant out-of-plane k-vector components (k_{z_i}), chosen to provide the proper energy, and that ARPES spectra may be approximated with the ($k_{\mathrm{z}_i} = \mathrm{const}$) slices of the 3D dispersion relation. We have applied this model on our data: the constants k_{z_i} are found by solving equations $E_{\mathrm{cb}}(k_{\mathrm{z}_i}^2) = E_{ci}$, E_{ci} being the discrete localization energies (for $\mathbf{K}_\parallel = 0$) in the quantum well. The localization energies are then obtained from the experimental data as $E_{ci} = -\mathrm{VBM} - E_g + E_i$, and the model subbands are evaluated as $E_i(k_{\mathrm{x}}) = E_{\mathrm{cb}}({k_{\mathrm{x}}}^2 + k_{\mathrm{z}_i}^2)$. $k_{\mathrm{y}} = 0$ is warranted by the experimental geometry. They are shown in Fig. 9 with black dashed lines. Although these lines follow approximately the lowest subbands, the model is disqualified due to the large disparities observed for the higher bands.

Here, we notice that the model assuming that the ($k_{\mathrm{z}_i} = \mathrm{const}$) slice of the 3D dispersion relation corresponds to the 2DEG dispersion is not correct for nonparabolic systems since, for such systems, partial energies cannot be associated with the Carthesian coordinates in the k space simply. The formally correct description of the 2DEG dispersion is obtained, e.g., with the Schrödinger-Poisson theory using the Thomas-Fermi approximation (SP/TF scheme), here with Eq. (11) in Sec. III. The 2DEG bands evaluated in this way are shown in Fig. 9(a) with the solid magenta lines. As seen, these theoretical lines agree reasonably well with the experimental bands for all subbands. The band-2 energies are typically slightly too large, which we think is caused by the applied approximations. This moderate discrepancy is not essential since, for the given sample, the band shapes only minimally change with their subband number, so they also have to be insensitive to corrections in theory, leading to small shifts on the energy scale. The shapes do not depend strongly on the band bending and λ, which are the most uncertain parameters within our SP description. Thus, the band-shape convergences are the most reliable indication of the correctness of this model. Going to the details, only the experimental band 1 of sample A deviates minimally when compared to its SP/TF model line. Although this could be a signature of spillout effect or *e-d* mass renormalization, this is on the verge of the experimental accuracy and, likely, such small difference can also be caused by approximations used in the model. Thus, we conclude that no mass renormalization arising due to *e-d* interactions is needed, and the InAs 2DEG bands are described with a one-electron SP/TF theory, with acceptable accuracy. The many-body interactions are revealed only by the band Lorentzian widths.

Finally, we return to the very close convergence of the fitted Kane model lines and the ARPES 2DEG bands. We emphasize here that the ARPES bands have a distinct 2D character (they show no k_z broadening and no dependence on photon energy), so they correspond directly to the $E_i(\mathbf{K}_\parallel)$ dispersion lines.

We have found that the Δ parameter, seen on the ARPES valence band spectra as the energy difference between VBM and so$|_{k=0}$, does not change with the 2DEG density (see Fig. 3, other densities not shown). With regard to E_g, the situation is not equally clear since E_g is not accessible with ARPES directly. In fact, band-gap narrowing (BGN) is expected for dense electron gases in semiconductors [80]. The BGN for 2DEG may be estimated based on the BGN for the corresponding 3D system from Ref. [80]. We read the 3D BGN for an equal Wigner-Seitz r_s parameter and scale it up 2–3 times, taking into account results obtained in Refs. [21,67]. The result for our sample A, for which the effect is the most pronounced, is 40–60 meV. We have also studied how far E_g may be reduced without compromising the Kane function [Eq. (1)] fits. For sample A this is 70 meV. The E_g reduction is compensated with an insignificant decrease in the m_{cb} (by 0.001 m_0) while the band shape is preserved.

Having this we see that the Kane fits shown in Fig. 9 involve the parameters E_g and Δ, which are the physical realities. The fits are obtained using the **kp** InAs conduction band model with adjusted electron effective mass only. Given the nearly perfect convergence of the fit lines and the experimental data, we suppose a physical significance of the Kane **kp** formalism, within the problem studied. Can it be understood further? We note here that the 2DEG wave functions occupy the crystal layer thick on atomic scale (tens up to a hundred atomic layers), and also the studied surface is unreconstructed, preserving the in-plane crystal periodicity up to the very surface, while the **kp** formalism involves, in the first place, the microscopic crystal potential.

The mathematically complex, theoretical picture of 2DEG bands [Eqs. (11) and (12)] arises within the SP/TF description scheme. Within this description, one uses the plane-wave representation of $\psi_\perp$ [Eq. (10)], so that the out-of-plane momentum components (k_n) are formally present. Then the 3D nonparabolic (nonseparable) dispersion relation [Eq. (1)] is involved causing the in-plane and out-of-plane parts of the problem to be not separated within this scheme.

On the other hand, for 2D systems, the out-of-plane momentum component is not a good quantum number, therefore, for the dispersion relation $E(\mathbf{K})$ (i.e., our observable) one writes simply: $E(\mathbf{K}) = E(\mathbf{K}_\parallel)$.

As we have mentioned in Sec. I the systems studied here do not depart far from the ideal two-dimensionality. Yet, they are quasi-2D, and they involve the out-of-plane energies. If the out-of-plane problem is completely separated, one can obviously write for the subbands i: $E_i(\mathbf{K}_\parallel) = E(\mathbf{K}_\parallel) + E_i$, where the $E(\mathbf{K}_\parallel)$ is the solution of the in-plane problem, meaning the identical subband shapes. However, for the case studied the nonseparability problem appears explicitly in the the SP/TF description. Therefore, it seems possible that the 2DEG system may inherit this property, despite the fact that the nonseparable 3D dispersion is not directly applicable for the system. Thus, it is not expected that, on the dispersion graphs, the 2DEG subbands will be shifted copies of some single line shape.

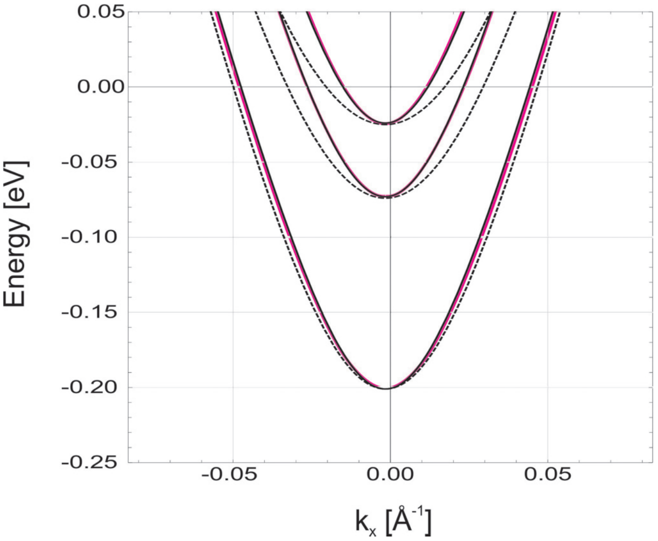

FIG. 10. A schematic comparison of the band model shapes discussed here. Solid black lines correspond to Kane band shape fitted to the experimental data (based on sample B, band 1). The same band shape for all three subbands is drawn (it fits all subbands within the experimental accuracy). Black dashed lines correspond to the slices of the 3D dispersion relation as proposed by Kawasaki *et al.* [24]. The magenta lines are Schrödinger-Poisson line shapes. These shapes differ insignificantly between different subbands and they are hardly discernible from the Kane line shapes. Such relations are observed for all studied samples (Fig. 9)

Paradoxically, the experimental InAs 2DEG subbands are described rather well with copies of a single line shape; see Fig. 9. Moreover, there are only marginal differences also in the theoretical SP/TF subband shapes (Figs. 9 and 10). Thus, the nonseparability problem seems to be present at a certain level of SP/TF mathematical representation, but not at the end, in the solutions.

Therefore, we think that, for the 2DEGs studied, there is possibly a description within the complete separation frame, in which the out-of-plane part leads to discrete energies, and adjustment of the in-plane effective mass. The idea of confinement-dependent band mass in 2D systems is present in the literature, for example, in the theoretical paper of Ekenberg [81]. In the paper the formula for a confinement-dependent parallel band mass in nonparabolic quantum wells is also given. In Fig. 11 we show calculated density distributions in real space for the studied 2DEGs. The distributions evidence large differences of the electrons confinement for different samples. Unfortunately, the results given in Ref. [81] involve a dependence of the mass on the subband number, and therefore it cannot be tailored to our systems.

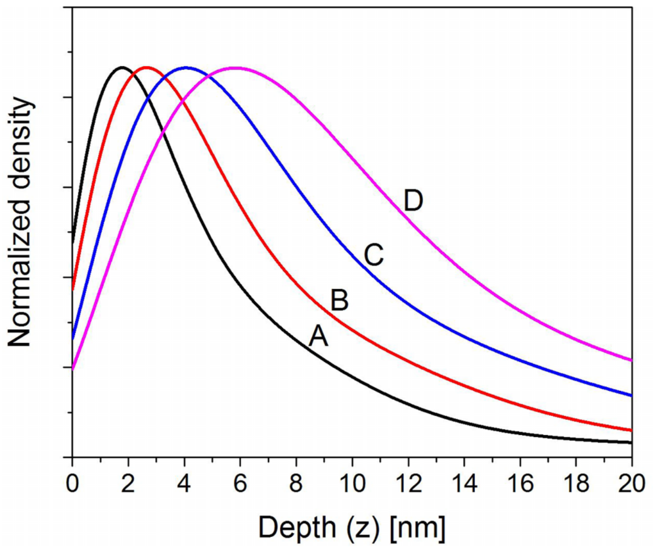

FIG. 11. Depth distributions of 2DEG electrons for the studied samples (see the labels associated with each curve), calculated within the Schrödinger-Poisson scheme. The distributions are obtained with an integration of the $\mathbf{K}_{\|}$-dependent contributions $[\psi_{\perp}^{i}(z, \mathbf{K}_{\|})]^2$ over the occupied $\mathbf{K}_{\|}$ space and a summation over all relevant subbands i. The distributions are shown normalized to their maxima.

On the other hand, a self-consistent Schrödinger-Poisson analysis of nonparabolic quantum well bands in InGaAs system (Ref. [82]) leads to results similar to ours, i.e., to subband shapes not differing significantly. So, our result may be very likely generalized for other nonparabolic systems. More work is needed, including experimental studies of 2DEGs on other nonparabolic crystals, to reach a more universal conclusion here.

V. CONCLUSIONS

There are several messages with which we would like to conclude this paper. The first is that the simple "const k_z" model is not sufficient for describing nonparabolic 2D electron systems. This is a general, sample-independent statement, which is also in line with the widely accepted notion that the k_z momentum is not a good quantum number in the context of 2D and quasi-2D systems.

The second message is that, in contrast to the previous result, the electron-electron interactions in InAs 2DEGs are weak and the most significant interactions of the many-body class are the electron-donor interactions. Still, no many-body renormalization of electronic bands is observed, and the bands are described well using the one-electron theoretical frame. Thus, we have to do with a "clean" model system in which many-body effects very weakly interfere with nonparabolicity. No significant spillout effects are present either.

A noticeably nontrivial observation for these model nonparabolic systems is also that they do not inherit the nonseparability of the in-plane and out-of-plane energies after its 3D matrix, i.e., the subbands do not differ in shape. They are convergent with the Kane **kp** band shape, obtained based on the bulk InAs Kane conduction band formula, with only the band-edge mass adjusted.

ACKNOWLEDGMENTS

The authors acknowledge the financial support of the Polish National Science Center-NCN under the Contract No. 2016/23/B/ST3/01140. J.J.K. thanks Prof. J. Konior for instructive discussions. A.M and M.G. thank Dr. J. Lis for providing initial scripts for Schrödinger-Poisson calculations.

---

[1] E. I. Chang, C.-I. Kuo, H.-T. Hsu, C.-Y. Chiang, and Y. Miyamoto, Appl. Phys. Express **6**, 034001 (2013).
[2] S. Mondal, G. C. Gardner, J. D. Watson, S. Fallahi, E. Yacoby, and M. J. Manfra, Solid State Commun. **197**, 20 (2014).
[3] I. Kostakis, D. Saeedkia, and M. Missous, IET Optoelectron. **8**, 33 (2014).
[4] S. A. Baig, J. L. Boland, D. A. Damry, H. H. Tan, C. Jagadish, H. J. Joyce, and M. B. Johnston, Nano Lett. **17**, 2603 (2017).
[5] J.-H. Hur and S. Jeon, Sci. Rep. **6**, 22001 (2016).
[6] *Advanced Indium Arsenide-based HEMT Architectures for Terahertz Applications*, edited by N. Mohankumar (CRC Press, Boca Raton, FL, 2022).
[7] J. D. Sau, R. M. Lutchyn, S. Tewari, and S. Das Sarma, Phys. Rev. Lett. **104**, 040502 (2010).
[8] J. Alicea, Phys. Rev. B **81**, 125318 (2010).
[9] R. M. Lutchyn, J. D. Sau, and S. Das Sarma, Phys. Rev. Lett. **105**, 077001 (2010).
[10] R. M. Lutchyn and L. I. Glazman, Phys. Rev. Lett. **119**, 057002 (2017).
[11] C. Thomas, A. T. Hatke, A. Tuaz, R. Kallaher, T. Wu, T. Wang, R. E. Diaz, G. C. Gardner, M. A. Capano, and M. J. Manfra, Phys. Rev. Mater. **2**, 104602 (2018).
[12] P. Virtanen, F. S. Bergeret, E. Strambini, F. Giazotto, and A. Braggio, Phys. Rev. B **98**, 020501(R) (2018).
[13] S. Lee, B. Shojaei, M. Pendharkar, A. P. McFadden, Y. Kim, H. J. Suominen, M. Kjaergaard, F. Nichele, H. Zhang, C. M. Marcus, and C. J. Palmstrøm, Nano Lett. **19**, 3083 (2019).
[14] C. Mittag, M. Karalic, Z. Lei, C. Thomas, A. Tuaz, A. T. Hatke, G. C. Gardner, M.J. Manfra, T. Ihn, and K. Ensslin, Phys. Rev. B **100**, 075422 (2019).
[15] Z. Lei, C. A. Lehner, E. Cheah, M. Karalic, C. Mittag, L. Alt, J. Scharnetzky, W. Wegscheider, I. Ihn, and K. Ensslin, Appl. Phys. Lett. **115**, 012101 (2019).
[16] L. Casparis, M. R. Conolly, M. Kjaergaard, N. J. Pearson, A. Kringhoj, T. W. Larsen, F. Kuemmeth, C. Thomas, S. Gronin, G. C. Gardner, M. J. Manfra, C. M. Marcus, and K. D. Petersson, Nat. Nanotechnol. **13**, 915 (2018).
[17] G. V. Graziano, J. S. Lee, M. Pendharkar, C. J. Palmstrom, and V. S. Pribiag, Phys. Rev. B **101**, 054510 (2020).
[18] D. Awschalom and N. Samarth, Physics **2**, 50 (2009).
[19] K. Premasiri and X. P. A. Gao, J. Phys.: Condens. Matter **31**, 193001 (2019)

[20] I. Martínez, P. Hogl, C. Gonzalez-Ruano, J. P. Cascales, C. Tiusan, Y. Lu, M. Hehn, A. Matos-Abiague, J. Fabian, I. Zutic, and F. G. Aliev, Phys. Rev. Appl. **13**, 014030 (2020).

[21] S. Das Sarma, R. Jalabert, and S.-R. Eric Yang, Phys. Rev. B **39**, 5516(R) (1989).

[22] N. Olszowska, J. Lis, P. Ciochon, L. Walczak, E. G. Michel, and J. J. Kolodziej, Phys. Rev. B **94**, 115305 (2016).

[23] P. D. C. King, T. D. Veal, C. F. McConville, J. Zúñiga-Pérez, V. Muñoz-Sanjosé, M. Hopkinson, E. D. L. Rienks, M. F. Jensen, and P. Hofmann, Phys. Rev. Lett. **104**, 256803 (2010).

[24] J. K. Kawasaki, C. H. Kim, J. N. Nelson, S. Crisp, C. J. Zollner, E. Biegenwald, J. T. Heron, C. J. Fennie, D. G. Schlom, and K. M. Shen, Phys. Rev. Lett. **121**, 176802 (2018).

[25] Y.-W. Tan, J. Zhu, H. L. Stormer, L. N. Pfeiffer, K. W. Baldwin, and K. W. West, Phys. Rev. Lett. **94**, 016405 (2005).

[26] W. Li, F. Giustino, Phys. Rev. B **101**, 035201 (2020).

[27] V. Umansky, M. Heilblum, Y. Levinson, J. Smet, J. Nubler, and M. Dolev, J. Cryst. Growth **311**1658 (2009).

[28] T. Tschirky, S. Mueller, C. A. Lehner, S. Fält, T. Ihn, K. Ensslin, and W. Wegscheider, Phys. Rev. B **95**, 115304 (2017).

[29] M. Noguchi, K. Hirakawa, and T. Ikoma, Phys. Rev. Lett. **66**, 2243 (1991).

[30] J. R. Weber, A. Janotti, and C. G. Van de Walle, Appl. Phys. Lett. **97**, 192106 (2010).

[31] M. J Lowe, T. D. Veal, C. F. McConville, G. R. Bell, S. Tsukamoto, and N. Koguchi, Surf. Sci. **523**, 179 (2003).

[32] V. Y. Aristov, G. Le Lay, V. M. Zhilin, G. Indlekofer, C. Grupp, A. Taleb-Ibrahimi, and P. Soukassian, Phys. Rev. B **60**, 7752 (1999).

[33] L. O. Olsson, C. B. M. Andersson, M. C. Hakansson, J. Kanski, L. Ilver, and U. O. Karlsson, Phys. Rev. Lett. **76**, 3626 (1996).

[34] T. D. Veal and C. F. McConville, Phys. Rev. B **64**, 085311 (2001).

[35] H. S. Karlsson, R. Viselga, and U. O. Karlsson, Surf. Sci. **402-404**, 590 (1998).

[36] M. G. Betti, V. Corradini, G. Bertoni, P. Casarini, C. Mariani, and A. Abramo, Phys. Rev. B **63**, 155315 (2001).

[37] See Supplemental Material at http://link.aps.org/supplemental/10.1103/PhysRevB.107.155139 for a brief discussion of sample surface stability during experiments, model EDC line shapes, and estimations of the spill-out effect.

[38] A. Bauer, M. Prietsch, S. Molodtsov, C. Laubschat, and G. Kaindl, Phys. Rev. B **44**, 4002 (1991).

[39] J. E. Demuth, W. J. Thompson, N. J. DiNardo, and R. Imbihl, Phys. Rev. Lett. **56**, 1408 (1986).

[40] M. Alonso, R. Cimino, and K. Horn, Phys. Rev. Lett. **64**, 1947 (1990).

[41] D. A. Evans, T. P. Chen, Th. Chasse, and K. Horn, Appl. Surf. Sci. **56-58**, 233 (1992).

[42] G. Paasch and H. Ubensee, Phys. Status Solidi B **113**, 165 (1982).

[43] H. Übensee, G. Paasch, J.-P. Zollner, and S. Handschack, Phys. Status Solidi B **147**, 823 (1988).

[44] H. Übensee, G. Paasch, and J. P. Zollner, Phys. Rev. B **39**, 1955 (1989).

[45] P. D. C. King, T. D. Veal, and C. F. McConville, Phys. Rev. B **77**, 125305 (2008).

[46] Lok C. Lew Yan Voon and M. Willatzen, *The k.p Method: Electronic Properties of Semiconductors* (Springer, Berlin, 2009), p. 56.

[47] Z. M. Fang, K. Y. Ma, D. H. Jaw, R. M. Cohen, and G. B. Stringfellow, J. Appl. Phys. **67**, 7034 (1990).

[48] We have adopted the most frequent value in the set provided in W. Nakwaski, Phys. B (Amsterdam) **210**, 1 (1995).

[49] Although the formula has been evaluated under assumption $\Delta \gg E_g$ it has been shown that it is applicable also for InAs semiconductor: A. Ya. Shul'man and D. V. Posvyanski, J. Exp. Theor. Phys. **130**, 903 (2020).

[50] E. O. Kane, J. Phys. Chem. Solids **1**, 249 (1957).

[51] G. Bonneau, J. Faraut, and G. Valent, Am. J. Phys. **69**, 322 (2001).

[52] S. Abe, T. Inaoka, and M. Hasegawa, Phys. Rev. B **66**, 205309 (2002).

[53] S. D. Kevan, Phys. Rev. Lett. **50**, 526 (1983).

[54] D. Pines and P. Nozieres, *The Theory of Quantum Liquids, Normal Quantum Liquids* (CRC Press, Boca Raton, FL, 2018).

[55] P. Hawrylak, G. Eliasson, and J. J. Quinn, Phys. Rev. B **37**, 10187 (1988).

[56] Y.-S. Kim, K. Hummer, and G. Kresse, Phys. Rev. B **80**, 035203 (2009).

[57] G. R. Bell, C. F. McConville, and T. S. Jones, Appl. Surf. Sci. **104-105**, 17 (1996).

[58] G. R. Bell, T. S. Jones, and C. F. McConville, Appl. Phys. Lett. **71**, 3688 (1997).

[59] G. E. Marques and I. J. Sham, Surf. Sci. **113**, 131 (1982).

[60] T. Balasubramanian, P. A. Glans, and L. I. Johansson, Phys. Rev. B **61**, 12709 (2000).

[61] G. Grimvall, *The Electron-Phonon Interactions in Metals* (North-Holland, New York, 1981).

[62] M. Hengsberger, R. Fresard, D. Purdie, P. Segovia, and Y. Baer, Phys. Rev. B **60**, 10796 (1999).

[63] J. E. Gayone, C. Kirkegaard, J. W. Wells, S. V. Hoffmann, Z. Li, and P. Hofmann, Appl. Phys. A **80**, 943 (2005).

[64] Within ARPES spectra, Frohlich interactions are seen as shake-up features separated from parent feature by multiples of the average LO phonon energy; Z. Wang, S. McKeown Walker, A. Tamai, Y. Wang, Z. Ristic, F. Y. Bruno, A. de la Torre, S. Ricco, N. C. Plumb, M. Shi, P. Hlawenka, J. Sänchez-Barriga, A. Varykhalov, T. K. Kim, M. Hoesch, P. D. C. King, W. Meevasana, U. Diebold, J. Mesot, B. Moritz, T. P. Devereaux, M. Radovic *et al.*, Nat. Mater. **15**, 835 (2016).

[65] T. Valla, A. V. Fedorov, P. D. Johnson, and S. L. Hulbert, Phys. Rev. Lett. **83**, 2085 (1999).

[66] J. J. Quinn and R. A. Ferrell, Phys. Rev. **112**, 812 (1958).

[67] G. Tränkle, H. Leier, A. Forchel, H. Haug, C. Ell, and G. Weimann, Phys. Rev. Lett. **58**, 419 (1987).

[68] A. T. Hatke, T. Wang, C. Thomas, G. C. Gardner, and M. J. Manfra, Appl. Phys. Lett. **111**, 142106 (2017).

[69] Q. Shi, S.A. Studenikin, M.A. Zudov, K.W. Baldwin, L.N. Pfeiffer, and K.W. West, Phys. Rev. B **93**, 121305(R) (2016).

[70] G. C. Gardner, S. Fallahi, J. D. Watson, and M. J. Manfra, J. Cryst. Growth **441**, 71 (2016).

[71] M. Sammon, T. Chen, and B. I. Shklovskii, Phys. Rev. Mater. **2**, 104001 (2018).

[72] While we see the effective mass asymptotic behavior within the measured r_s range, we do not claim that this behavior continues far beyond this range. Theoretical indications are divergent in this question; see for example R. Asgari, B. Davoudi, and B. Tanatar, Solid State Commun. **130**, 13 (2004), some predict a strong increase in effective mass at low densities. However,

increasing mass, as well as other complications (e.g., Wigner crystallization), seems to be possible for densities far lower than the ones studied here.

[73] R. Asgari, B. Davoudi, M. Polini, G. F. Giuliani, M. P. Tosi, and G. Vignale, Phys. Rev. B **71**, 045323 (2005).

[74] G. D. Mahan, J. Appl. Phys. **51**, 2634 (1980).

[75] S. C. Jain and D. J. Roulston, Solid-State Electron. **34**, 453 (1991).

[76] D. M. Szmyd. P. Porro, and A. Majerfeld, J. Appl. Phys. **68**, 2367 (1990).

[77] I. Te Lu, J.-J. Zhou, and M. Bernardi, Phys. Rev. Mater. **3**, 033804 (2019).

[78] N. Schildermans, M. Hayne, V. V. Mosnchlkov, A. Rastelli, and O. G. Schmidt, Phys. Rev. B **72**, 115312 (2005).

[79] G. W. Gobeli and F. G. Allen, Phys. Rev. **137**, A245 (1965).

[80] V. Palankovski, G. Kaiblinger-Grujin, and S. Selberherr, Mater. Sci. Eng. B **66**, 46 (1999).

[81] U. Ekenberg, Phys. Rev. B **40**, 7714 (1989).

[82] L. Wang, P. M. Asbeck, and Y. Taur, Solid-State Electron. **54**, 1257 (2010).

Correction: A proof change request was not implemented properly in the eighth paragraph of Sec. IV F and has been set right.